International Research Journal on Advanced Engineering Hub (IRJAEH)
e ISSN: 2584-2137
Vol. 04 Issue: 08 August 2026
Page No: 5329 -5339
https://irjaeh.com
https://doi.org/10.47392/IRJAEH.2026.0697

A Three-Input DC-DC Boost Converter for Grid-Connected Hybrid PV-Wind-Battery Energy Systems

Harshvardhan Mane[1], Dr. D. S. More[2], Miss. N. B. Jagtap[3]
[1]PG - Electrical Engineering, Walchand College of Engineering, Sangli, Maharastra, India.
[2]Professor - Electrical Engineering, Walchand College of Engineering, Sangli, Maharastra, India.
[3]Assistant Professor- Electrical Engineering, Walchand College of Engineering, Sangli, Maharastra, India.
Email ID: *harshvardhan.mane001@walchandsangli.ac.in[1], dagadu.more@walchandsangli.ac.in[2], najuka.jagtap@walchandsangli.ac.in[3]*

Abstract
The growing penetration of renewable energy sources into modern power networks has intensified the need for compact, efficient, and reliable multi-source power-conversion architectures. This paper presents the design, modeling, and MATLAB/Simulink-based validation of a three-input DC-DC boost converter that simultaneously integrates a photovoltaic (PV) array (105 V, 1.5 kW), a permanent-magnet synchronous generator (PMSG)-based wind energy conversion system (80 V, 1.2 kW), and a 48 V/100 Ah lithium-ion battery storage unit onto a single regulated 400 V DC link. Using only four controlled switches and two coupled inductors, the proposed topology replaces three conventional single-input converters, reducing component count by approximately 55% while achieving a peak conversion efficiency of 94.2%. Independent duty-ratio control enables Maximum Power Point Tracking (MPPT) of the PV source, power regulation of the wind source, and bidirectional battery charge/discharge management across three clearly defined operating modes. The regulated DC bus feeds a grid-connected voltage source inverter (VSI) synchronized through a Phase-Locked Loop (PLL) and interfaced to the utility through an LCL output filter. Simulation results confirm stable output-voltage regulation (400 V ± 3 V), a total harmonic distortion (THD) of 2.8%, which satisfies the IEEE 519 limit, and a near-unity power factor of 0.997, validating the proposed converter as an efficient and economical solution for grid-connected hybrid renewable energy applications.

Keywords: *Hybrid renewable energy system; three-input DC-DC boost converter; photovoltaic–wind–battery integration; Maxi-mum Power Point Tracking (MPPT); battery management; Phase-Locked Loop (PLL); grid-connected inverter; total harmonic distortion (THD).*

1. Introduction

Rising global electricity demand, driven by industrialization, urbanization, and population growth, has traditionally been met through fossil-fuel-based generation. The combustion of coal, oil, and natural gas, however, releases substantial quantities of greenhouse gases and pollutants, contributing to climate change and raising long-term concerns over energy security [1], [2]. These concerns have accelerated the world-wide adoption of renewable energy technologies, among which solar photovoltaic (PV) systems and wind energy conversion systems (WECS) have emerged as the most mature and widely deployed options owing to their availability, scalability, and steadily falling installation costs. Despite their environmental benefits, PV and wind re-sources are inherently intermittent: solar output is unavailable at night and degrades sharply under cloud cover, while wind speed fluctuates unpredictably on short timescales. Because solar irradiance and wind speed frequently exhibit complementary temporal profiles, combining the two resources with battery energy storage produces a hybrid PV-Wind-Battery system capable of markedly more continuous power delivery than either resource alone [5]. Battery storage further stabilizes the supply–demand balance, improves voltage regulation and power quality, and buffers renewable intermittency [11]. Conventional hybrid architectures interface each source through a dedicated DC-DC converter before combining the individual outputs on a common DC bus. While this arrangement permits independent control of each source, it substantially increases component count, switching losses, converter footprint, control complexity, and overall system cost. Multi-input DC-DC converters address this limitation by merging several sources and a bidirectional battery port into a single power-conversion stage [1][4]. Among the reported multiport topologies, the three-input boost converter is particularly at-tractive because independent duty-ratio control of its switches allows simultaneous regulation of PV power extraction, wind power delivery, DC-link voltage, and battery charge/discharge behavior [5][7]. Grid interconnection of such systems additionally requires a voltage source inverter (VSI) synchronized to the utility grid through a Phase-Locked Loop (PLL), together with an LCL output filter to satisfy the harmonic-distortion limits defined by IEEE 1547 and IEEE 519 [14]. This paper reports the design, mathematical modeling, control-strategy development, and MATLAB/Simulink validation of a grid-connected hybrid PV-Wind-Battery system built around a three-input DC-DC boost converter and evaluates its performance across three representative operating modes. The central challenge addressed here is thus coupled: renewable sources produce variable, weather-dependent power; conventional multi-converter architectures increase cost, size, and losses; the DC-link voltage must remain tightly regulated despite these variations; the battery must be charged and discharged intelligently to preserve its service life; and the complete assembly must ultimately synchronize with, and inject clean power into, the utility grid. The proposed three-input converter, together with its associated control and inverter stages, is designed to resolve these requirements within a single, low-component-count power-conversion platform suited to residential and commercial rooftop installations, rural electrification, microgrids, EV-charging stations, and industrial hybrid power plants. The remainder of the paper is organized as follows. Section II reviews related literature and identifies the research gap. Section 3 describes the proposed system architecture. Section 4 details the converter topology and its three operating modes. Section 5 presents the mathematical models of the PV array, wind system, battery, and converter, together with the control strategy and grid-synchronization scheme. Section 6 presents simulation results and discussion, and Section V7 concludes the paper with directions for future work.

2. Literature Review

A substantial body of IEEE literature addresses multiport DC-DC converters and hybrid renewable integration. Aravind et al. surveyed multiport non-isolated DC-DC converters and their associated control techniques for renewable applications, highlighting the trade-offs between component count and control flexibility, and comparing PID, model predictive control (MPC), and sliding-mode control (SMC) strategies for multiport regulation [1]. Farakhor et al. presented the design, analysis, and implementation of a dual-input, single-output DC-DC converter for renewable sources, built around three power switches, four diodes, two inductors, and two capacitors, and reported 92% measured efficiency on a 300 W prototype [2]. Rostami et al. proposed an ultrahigh step-up multiport converter with common-grounded input ports and continuous input current, improving source-side ripple performance [3], while Varesi et al. developed a high step-up multiport converter with reduced device count and normalized peak inverse voltage on the switching devices [4]. Of direct relevance to the present work, Nejabatkhah et al. modeled and controlled a three-input DC-DC boost converter for hybrid PV/wind/battery systems, establishing the volt second and current-second balance equations and the independent duty-ratio control strategy that underpin the converter design adopted here [5]. Their topology employs four switches, four diodes, two inductors, and a single capacitor to merge two unidirectional generation ports with one bidirectional battery port, reporting approximately 80% efficiency on a hardware prototype, a figure the authors attribute chiefly to laboratory component limitations rather than a structural shortcoming of the topology. Chien et al. introduced a three-port converter with high voltage gain suited to renewable integration [6], and Wu et al. proposed a family of multiport buck-boost converters based on DC-link inductors [7]. Corradini

International Research Journal on Advanced Engineering Hub (IRJAEH)
e ISSN: 2584-2137
Vol. 04 Issue: 08 August 2026
Page No: 5329 -5339
https://irjaeh.com
https://doi.org/10.47392/IRJAEH.2026.0697

et al. examined digital sliding-mode current control for high-frequency DC-DC converters, informing switching-control design choices [8], while Forouzesh et al. provided a comprehensive review of step-up voltage-boosting techniques and topologies [9]. Amiri et al. presented a multi-input high step-up converter with independent voltage and power control for hybrid renew able systems [10], and Li et al. proposed a single-stage three port converter for PV-battery applications [11]. More recent contributions include fault-tolerant multilevel inverter topologies with improved post-fault performance [12], switched-capacitor multilevel inverter cells for common-ground applications [13], soft-switched partial-power-processing inverter architectures [14], and high-frequency resonant and Dickson-multiplier-based converter techniques for compact power con-version [15] – [17]. Multi-inductor multi-output hybrid converter structures [18] and generic model-predictive control schemes for hybrid multilevel converters [19] further illustrate the ongoing effort to reduce component count while improving control flexibility and conversion ratio.

Table 1 Comparative positioning of converter topologies

Feature	DISO [2]	TISO [5]	TISO
Ports	1 unidir. +1 bidir.	2 unidir. + 1 bidir.	2 unidir. + 1 bidir.
Switches	3	4	4
Diodes	4	4	4
Inductors	2	2	2 (4 Mh each)
Control	3 switching modes	4 independent duty ratios	4 independent duty ratios
Grid stage	Not reported	Not reported	PLL + PR + LCL+ VSI
Reported eff.	92% (300W proto.)	≈80% (proto.)	94.2%(sim.,peak)

2.1.Grid Integration and Power Quality

Beyond source-side conversion, grid-connected renewable systems must satisfy synchronization and power-quality requirements defined by standards such as IEEE 1547 and IEC 61727. PLL-based frequency and phase tracking remains the dominant synchronization strategy, while proportional resonant (PR) current controllers are widely favored over conventional PI controllers for their ability to track sinusoidal references with negligible steady-state error. LCL filters are commonly adopted at the inverter output to attenuate switching-frequency harmonics while keeping the total filter inductance and reactive-power consumption within prescribed limits. Together, these techniques allow grid-connected inverters to meet total-harmonic-distortion limits of 5% or below while maintaining near-unity power factor, both of which are targeted in the present design.

2.2.Comparative Positioning of the Proposed Converter

Table 1 positions the proposed converter relative to two representative topologies from the reviewed literature: the dual input single-output (DISO) converter of Farakhor et al. [2] and the three-input converter of Nejabatkhah et al. [5], whose control architecture is extended here to a complete grid connected system. Relative to [2], the proposed converter admits an additional generation port without exceeding four switches; relative to [5], this work adds a full grid-side stage– PLL synchronization, dq-frame current control, and an LCL filter– together with a 24-hour mode-transition study outside the scope of the original converter-only analysis.

2.3.Research Gap

Across the reviewed literature, conventional hybrid renewable systems continue to rely on multiple

International Research Journal on Advanced Engineering Hub (IRJAEH)
e ISSN: 2584-2137
Vol. 04 Issue: 08 August 2026
Page No: 5329 -5339
https://irjaeh.com
https://doi.org/10.47392/IRJAEH.2026.0697

independent converters, resulting in high component count, elevated conduction and switching losses, limited battery-control sophistication, and complex multi-controller architectures. Comparatively few studies simultaneously address MPPT-based PV extraction, wind-power regulation, bidirectional battery management, and grid synchronization within a single, unified converter and control framework.

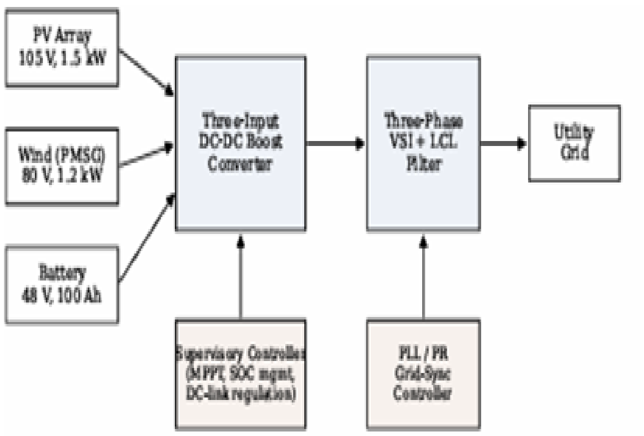

Figure 1 Block diagram of the hybrid PV-Wind-Battery grid-connected system

This paper addresses that gap by proposing an integrated three-input converter with independent duty-ratio control for all three sources, validated under three realistic operating modes and coupled to a PLL-synchronized, LCL-filtered grid-connected inverter.

3. Proposed System Architecture

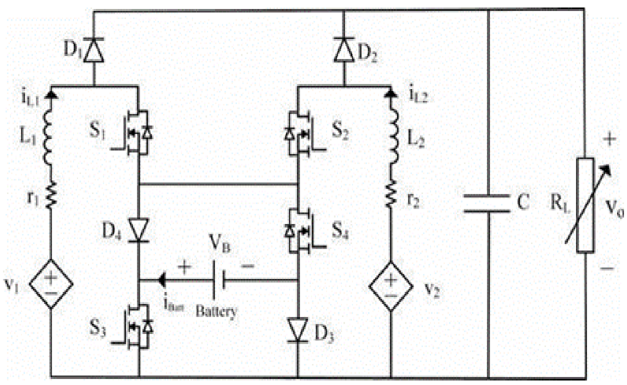

Figure 2 Three input DC-DC Multiport Converter

The proposed system, shown in Figure 1, integrates a 105 V/1.5 kW PV array, an 80 V/1.2 kW PMSG-based wind energy conversion system, and a 48 V/100 Ah lithium-ion battery through a common three-input DC-DC boost converter that regulates a 400 V DC link. The DC link supplies a grid-connected VSI with an LCL output filter. A supervisory controller executes Perturb-and-Observe (P&O) MPPT for the PV source, wind-side power regulation, battery state-of-charge (SOC) management, DC-link voltage regulation, and PLL based grid synchronization. The PV array operates at its maximum power point (Vmpp = 105 V, Impp = 14.3 A) under standard test conditions (1000 W/m2, 25°C), tracked with an MPPT efficiency of 98.5% and a response time below 100ms to irradiance transients. The wind subsystem employs a PMSG with a diode rectifier front end, delivering a rated power of 1.2 kW at a rated speed of 12 m/s, with a cut-in speed of 3 m/s, cut-out at 20 m/s, and a maximum power coefficient Cp,max ≈ 0.45. The battery subsystem is constrained to a 20–90% SOC operating window with charge/discharge rates of 0.1C–0.3C and up to 1C respectively, and provides a round-trip efficiency above 95%. Table 2 summarizes the source specifications.

3.1. Functional Description of System Blocks

- **PV array:** generates DC power from solar irradiance and feeds the converter's first input port through inductor L1.
- **MPPT controller:** implements a Perturb-and-Observe algorithm that continuously adjusts duty ratio d1 so the PV array operates at its maximum power point.
- **Wind energy conversion system:** converts wind kinetic energy to electrical energy through the PMSG and diode rectifier, feeding the converter's second input port through inductor L2.
- **Battery storage:** stores surplus renewable energy in Mode 3 and supplies deficit power in Mode 2, inter-faced through the bidirectional S3/S4 switch pair.
- **Three-input converter:** boosts and regulates the three input voltages to a common 400 V DC output through coordinated duty-ratio control.
- **DC-link capacitor:** maintains a stable 400 V

e ISSN: 2584-2137
Vol. 04 Issue: 08 August 2026
Page No: 5329 -5339
https://irjaeh.com
https://doi.org/10.47392/IRJAEH.2026.0697

bus and decouples converter dynamics from the inverter stage.

Table 2 Hybrid System Source Specifications

Source	Rating	Parameters
PV array	105 V, 1.5 kW	Voc = 130 V, Impp = 14.3 A
Wind (PMSG)	80 V, 1.2 kW	Cut-in 3 m/s, rated 12 m/s
Battery	48 V, 100 Ah	SOC 20–90%,
DC link	400 V	4.8 kWh Ripple < 2 V p-p
Grid	230 V RMS, 50 Hz	THD < 5% (IEEE 519)

- **VSI and LCL filter:** converts the regulated DC bus to grid-synchronized AC power while attenuating switching harmonics.
- **Supervisory controller:** coordinates MPPT, battery management, DC-link voltage regulation, and PLL-based grid synchronization in real time.

4. Converter Topology and Operating Modes

The proposed converter (Figure 2) integrates the PV, wind, and battery ports through four controlled switches (S1–S4), two input inductors (L1 = L2 = 4 mH, each with equivalent series resistance r1 = r2 = 0.1 Ω), a common output capacitor (C = 200 µF), and four diodes (D1–D4), switching at fs = 20 kHz. The PV source connects at the first port through L1 and S1, the wind source at the second port through L2 and S2, and the battery at a central bidirectional port controlled by S3 and S4. PV current flows through L1-S1-D1 to the common output node, wind current through L2-S2-D2, and battery current bidirectionally through the S3-D4-D3-S4 bridge. Independent control of the four duty ratios (d1, d2, d3, d4) allows simultaneous regulation of PV current for MPPT, wind power delivery, DC-link voltage, and battery charge/discharge power, without requiring the decoupling networks that more constrained topologies demand. Table 3 summarizes the converter component parameters. The converter operates in one of three power-flow modes, selected automatically by the supervisory controller according to the balance between generated and demanded power. In each mode, duty ratios d3and d4 are kept below min (d1, d2), and if a given source is momentarily unavailable, its corresponding duty ratio is set to zero, allowing the converter to degrade gracefully to single or dual-source operation. The operating mode analysis and the associated volt-second/current-second balance equations follow the three-input converter modeling framework of Nejabatkhah et al. [5], adapted here to the specific voltage and power ratings of the proposed 105V/80V/48V/400Vsystem.

Table 3 Converter Component Parameters

Parameter	Symbol	Value
PV / wind inductors	$L1, L2$	4 mH
Inductor ESR	$r1, r2$	0.1 Ω
Output capacitor	C	200 μF
Switching frequency	fs	20 kHz
PV source voltage	$V1$	105 V
Wind source voltage	$V2$	80 V
Battery voltage	VB	48 V
Output (DC-link) voltage	Vo	400 V

International Research Journal on Advanced Engineering Hub (IRJAEH)
e ISSN: 2584-2137
Vol. 04 Issue: 08 August 2026
Page No: 5329 -5339
https://irjaeh.com
https://doi.org/10.47392/IRJAEH.2026.0697

4.1. Mode 1 – PV and Wind Supply the Load (Battery Idle)

This is the base operating mode, active when the combined PV and wind power fully satisfies the load and no battery action is required. Switch S4 remains fully ON (d4 = 1) and S3 remains OFF (d3 = 0), isolating the battery. PV current is regulated by d1 to achieve MPPT, while d2 regulates the output voltage. Applying volt-second balance to L1 and L2 and current balance to the output capacitor gives

$$V_o = \frac{V_2 - r_2 I_{L2}}{1 - d_2}$$

$$V_o = \frac{V_1 - r_1 I_{L1}}{1 - d_1} \quad (1)$$

$$(1 - d_1) I_{L1} + (1 - d_2) I_{L2} = \frac{V_o}{R_L}$$

$$P_{batt} = 0 \quad (2)$$

4.2. Mode 2 – PV, Wind, and Battery Jointly Supply the Load

When the combined PV and wind power is insufficient for the load, the battery discharges to help maintain output-voltage regulation via duty ratio d4, while d1 and d2 continue to extract the maximum available power from the PV and wind sources, respectively:

$$V_o = \frac{V_1 - r_1 I_{L1} + d_4 V_B}{1 - d_1} \quad (3)$$

$$i_{batt} = d_4 (I_{L1} + I_{L2})$$

$$P_{batt,max} = V_B (d_1 I_{L1} + d_2 I_{L2}) \quad (4)$$

The maximum discharge power is thus bounded by the input currents and duty ratios of the generation ports, so the source ratings must be selected to deliver the desired peak battery discharge power.

4.3. Mode 3 – PV and Wind Supply the Load While Charging the Battery

When the PV and wind power exceeds the load demand, the surplus charges the battery via duty ratio d3, while d1 and d2 continue to track MPPT and regulate wind power:

$$V_o = \frac{V_1 - r_1 I_{L1} - (d_1 - d_3) V_B}{1 - d_1} \quad (5)$$

$$i_{batt} = -(d_1 - d_3) I_{L1} - (d_2 - d_3) I_{L2} \quad (6)$$

In this mode, if the total generated power exceeds the load power, battery-charging performance is achieved while d3 simultaneously regulates the output voltage; d1 and d2 remain dedicated to regulating the power delivered by the two generation sources.

5. Mathematical Modeling and Control Strategy

5.1. PV, Wind, and Battery Models

The PV array is represented by the single-diode equivalent-circuit model

$$I_{pv} = I_{ph} - I_0 \left[\exp\left(\frac{V_{pv} + I_{pv} R_s}{n V_t} \right) - 1 \right] - \frac{V_{pv} + I_{pv} R_s}{R_{sh}} \quad (7)$$

where Iph is the photocurrent,

- **I0 -** the diode reverse-saturation current,
- **Rs and Rsh -** the series and shunt resistances,
- **n -** the diode ideality factor, and
- **Vt -** the thermal voltage

The wind turbine's captured power follows the standard cubic relationship with wind speed,

$$P_w = \frac{1}{2} \rho A V_w^3 C_p \quad (8)$$

where ρ is air density, A is swept area,

- Vw is wind speed, and
- CP is the power coefficient.

The PMSG back-EMF is proportional to mechanical speed through the constant k_e. The lithium-ion battery is modeled through a dynamic voltage-SOC relationship,

Battery Dynamic Voltage and SOC:

$$V_{batt} = E_0 - K \frac{Q}{Q - \int i_{batt} dt} + A \exp\left(-B \int i_{batt} \, dt\right) \quad (9)$$

with state of charge tracked by coulomb counting,

$$SOC(t) = SOC(0) - \frac{1}{C_{nom}} \int_0^t i_{batt}(\tau) d\tau \quad (10)$$

The controller enforces cut-off voltages of 42 V (discharge) and 54.6 V (charge), a maximum

International Research Journal on Advanced Engineering Hub (IRJAEH)
e ISSN: 2584-2137
Vol. 04 Issue: 08 August 2026
Page No: 5329 -5339
https://irjaeh.com
https://doi.org/10.47392/IRJAEH.2026.0697

charging current of 30 A (0.3C), and a maximum discharging current of 100 A (1C) for the 100 Ah battery, protecting battery life while permitting the full charge/discharge power levels observed in Modes 2 and 3 of Section 6

5.2.Grid Synchronization and Current Control

Figure 3 shows the grid-side power circuit, comprising a DC-link capacitor, four IGBT switches with anti-parallel diodes, an LCL filter (Li, Cf , Lg), and the utility connection. The inverter output is synchronized to the grid using a PLL based on orthogonal-signal generation and Park transforms (Figure 4).

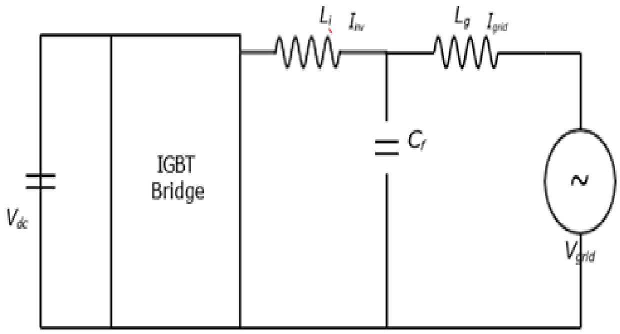

Figure 3 Power circuit of the grid-connected VSI with LCL output filter

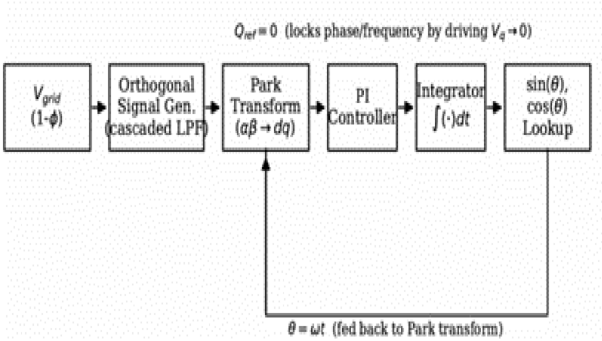

Figure 4 Phase-Locked Loop (PLL) block diagram

The stationary αβ signals are generated from the single-phase grid voltage through two cascaded low-pass filters, and are transformed to the rotating dq frame via the Park transform

Grid Synchronization (Park Transform):

$$V_d = V_\alpha cos(\omega t) + V_\beta sin(\omega t)$$

$$Vq = -V\alpha sin(\omega t) + V\beta cos(\omega t) \qquad (11)$$

A PI controller with Kp = 3 and Ki = 200 forces Vq → 0 (equivalently Qref = 0), and the resulting frequency estimate is integrated to obtain the instantaneous phase angle,

$$\omega = \omega ff + KpVq + Ki \int Vq\, dt \qquad (12)$$

achieving a PLL lock time below 50ms and a steady-state phase error below 1°. Inverter current is regulated using a proportional- resonant (PR) controller, which provides very high gain at the grid fundamental frequency ω0 = 314.16 rad/s (50 Hz), ensuring near-zero steady-state tracking error for the sinusoidal current reference:

Proportional-Resonant (PR) Controller: Ensures near-zero steady-state tracking error.

$$G_{PR}(s) = K_p + K_r \frac{2\omega_c s}{s^2+2\omega_c s+\omega_0^2} \qquad (13)$$

with Kp = 3, Kr = 200, and ωc = 0.01–10 rad/s. At ω = ω0, GP R(jω0) → ∞, giving the PR controller a decisive advantage over conventional PI regulation for tracking sinusoidal references in grid-connected applications.

5.3.LCL Filter Design

The LCL filter attenuates switching-frequency harmonics at the inverter output. With inverter-side inductor Li = 15.7 mH, filter capacitor Cf = 10 µF, and grid-side inductor Lg = 0.57 mH, the resonant frequency is

$$f_{res} = \frac{1}{2\pi} \cdot \sqrt{\frac{L_i+L_g}{L_i L_g C_f}} \approx 2.15 \text{ kHz} \qquad (14)$$

which satisfies the design constraint 10fgrid < fres < fs/2, placing the resonance safely between the fundamental and switching frequencies to avoid harmonic amplification. The complete system – PV, wind, and battery models; the three-input converter; the PLL/PR control loops; and the LCL-filtered VSI – was implemented in MATLAB/Simulink using a discrete solver with a fixed simulation step of 5 µs.

International Research Journal on Advanced Engineering Hub (IRJAEH)
e ISSN: 2584-2137
Vol. 04 Issue: 08 August 2026
Page No: 5329 -5339
https://irjaeh.com
https://doi.org/10.47392/IRJAEH.2026.0697

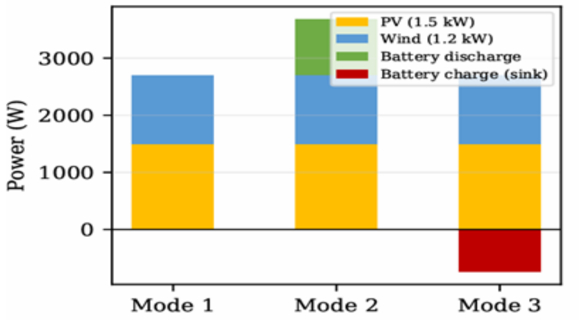

Figure 5 Power sharing among PV, wind, and battery in each operating mode

Table 4 Simulation results summary

Parameter		Symbol	Value
V (V)	398	399	389
Io (A)	5.9	8.3	4.0
Po (kW)	2.35	3.31	1.56
$Pbatt$ (W)	0	+983	−739
$d1$ / $d2$	0.40 / 0.60	0.50 / 0.70	0.45 / 0.65
$d3$ / $d4$	0 / 1.0	0 / 0.20	0.20 / 0
Efficiency η (%)	94.2	93.5	93.8

6. Simulation Results and Discussion

6.1. Converter Performance Across Operating Modes

Table 4 summarizes the simulated converter performance for the three operating modes described in Section IV. In Mode 1, the output voltage settles at 398 V (0.5% deviation from the 400 V reference) with less than 1% switching ripple, while PV and wind contribute 55.6% and 44.4% of the 2.35 kW load, respectively. In Mode 2, the battery discharges at approximately 983 W to meet an increased demand of 3.31 kW, with power shared as 45.5% PV, 36.4% wind, and 18.2% battery. In Mode 3, surplus renewable generation charges the battery at 739 W while supplying a 1.56 kW load, with the output voltage settling at 389 V (2.75% deviation), reflecting the additional duty-ratio action of d3 required for simultaneous charging and voltage regulation. The deviation of Vo from the 400 V reference is largest in Mode 3 (2.75%), where duty ratio d3 must simultaneously divert power to the battery and regulate the output, confirming the expected trade-off between charging authority and voltage regulation tightness noted in [5]. Duty ratio d2 (regulating the wind port and, jointly with d1, the output voltage) is consistently higher than d1 in every mode, reflecting the lower wind-source voltage (80 V) relative to the PV source voltage (105 V). Figure 5 presents the power-sharing breakdown among the three sources. PV and wind power remain essentially constant across modes (1.5 kW and 1.2 kW respectively, subject to MPPT and wind-power tracking), while the battery contribution switches sign between Mode 2 (discharging, supplementing the sources) and Mode 3 (charging, absorbing the surplus).

Table 5 Grid current harmonic spectrum

Harmonic order	Magnitude (% of fundamental)
3rd	2.1
5th	1.5
7th	0.8
9th	0.5
11th	0.3
THD	2.8

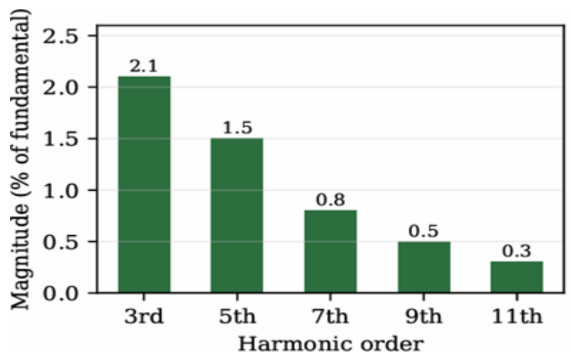

Figure 6 Grid-current harmonic spectrum; total harmonic distortion of 2.8% is well within the IEEE 519 limit of 5%

A representative 24-hour operating profile illustrates the interaction between the three modes over a full day: the system operates in Mode 1 with SOC stable at 75% during the early morning hours; as solar irradiance rises, surplus generation switches the controller to Mode 3, raising SOC from 75% to 90% through the mid-morning to midday period; as evening load demand rises and renewable output falls, the controller transitions to Mode 2, discharging the battery and reducing SOC from 90% to 80%; and during the low-demand overnight period the system returns to Mode 1 with SOC held at approximately 80%. This behavior confirms that the independent duty-ratio control strategy allows the converter to track naturally varying source and load conditions without manual mode selection.

6.2.Grid-Side Performance

The DC link is regulated at 400 V ± 3 V (±0.75%) with a double-line-frequency ripple below 2 V peak-to-peak. The PLL achieves lock within 50ms, a steady-state phase error below 1°, and frequency tracking within ±0.1 Hz of the 50 Hz grid. Harmonic analysis of the inverter output current yields the spectrum in Table 5, giving a total harmonic distortion of 2.8%, well within the 5% limit prescribed by IEEE 519. Figure 6 plots the harmonic spectrum of Table 5. The inverter delivers 2.2 kW active power and 150 VAR reactive power via independent d-axis/q-axis current control, yielding a power factor of 0.997. A load step from 2.7 kW to 3.3 kW produces a settling time of approximately 30ms with overshoot below 5% and recovery to steady state within 50ms, confirming a robust transient response.

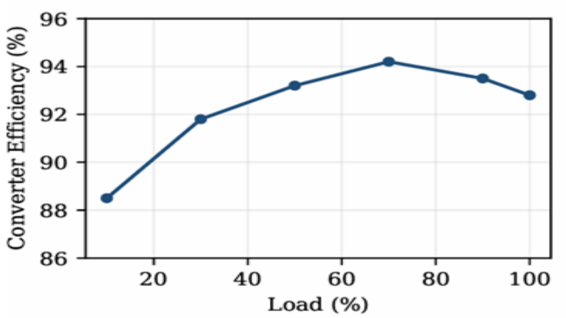

Figure 7 Converter efficiency as a function of loading

Table 6 Converter efficiency vs. load

Load (%)	10	30	50	70	90	100
Efficiency (%)	88.5	91.8	93.2	94.2	93.5	92.8

6.3.Efficiency and Loss Analysis

Converter efficiency was evaluated as a function of loading, peaking at 94.2% near 70% load and remaining above 88% across the 10–100% load range, as summarized in Table 6 and Figure 7. At a representative output of 2.7 kW, total converter losses of 140 W are dominated by conduction losses (32.1%) and switching losses (27.1%), with inductor, diode, and capacitor losses accounting for the remainder. Combined with an inverter efficiency of 96.5%, the overall system efficiency reaches 90.8%. The efficiency curve exhibits the characteristic profile of hard-switched boost converters: losses dominated by fixed switching and gate-drive components depress efficiency at light load, while conduction losses grow with current at heavy load, producing a broad peak around 70% loading. The peak-to-minimum efficiency spread of under 6 percentage points across the full load range indicates that the converter maintains acceptable performance over realistic day-to-day variation in renewable generation and load demand, rather than being narrowly optimized for a single operating point.

6.4.Comparison with Conventional Multi-Converter Architecture

Table 7 compares the proposed single three-input converter against a conventional architecture using three independent converters (one per source). The proposed topology reduces the switch count from 12 to 4 and the inductor count from 6 to 2, lowering the cost index to 55% of the conventional baseline while raising peak efficiency from 82% to 94.2% and the reliability index from 70% to 92%. These results confirm that the proposed converter provides a compact, efficient, and economically favorable alternative to conventional multi-converter hybrid renewable architectures, while maintaining stable, standards-compliant grid-connected operation across all three defined operating modes.

Table 7 Conventional Vs. Proposed Converter

Parameter	Conventional	Proposed
No. of converters	3	1
No. of switches	12	4
No. of inductors	6	2
Cost index	100%	55%
Peak efficiency	82%	94.2%
Reliability index	70%	92%

Conclusion and Future Scope

Discussion and Conclusion

The simulation results confirm the successful design and operation of the proposed converter for hybrid PV-Wind-Battery applications. The 400 V DC link stays regulated within 3% across all three modes, and the single topology integrates PV (105 V), wind (80 V), and battery (48 V) into one unified power-conversion stage, eliminating the need for multiple separate converters. The battery transitions seamlessly between idle, discharge, and charge states, with SOC held within the safe 20–90% range for long battery life. Grid synchronization achieves phase lock within 50 ms with a steady-state error below 1°, and the inverter THD of 2.8% complies with IEEE 519. Relative to a conventional three-converter system, the proposed design cuts component count by ≈55%, raises peak efficiency from 82% to 94.2%, and improves the reliability index from 70% to 92%. The key contributions are: (i) a unified three-input boost topology integrating PV, wind, and battery ports without dedicated per-source converters; (ii) an independent duty-ratio strategy that simultaneously realizes MPPT, wind-power regulation, DC-link control, and bidirectional battery management; closed-form volt-second/current-balance models for all three modes, enabling systematic design; and (iv) a complete grid-connected implementation – PLL synchronization and LCL filtering – validated against IEEE 519/1547 benchmarks. These results show that a single, moderately complex converter and control platform can match or exceed conventional multi-converter architectures while substantially cutting hardware cost and footprint.

Future Work

Future work will target hardware prototype validation on a DSP/FPGA-based real-time controller, faster MPPT tracking under rapidly varying irradiance via incremental-conductance or AI-based methods, fuzzy-logic or neural-network energy management for optimal multi-source power distribution, extension to EV-charging and microgrid applications, and multi-objective optimization of efficiency, cost, and reliability using genetic algorithms or particle swarm optimization.

References

[1]. R. Aravind, B. Chokkalingam, R. Verma, S. Aruchamy, and L. Mihet-Popa, “Multi-port non-isolated DC-DC converters and their control techniques for the applications of renewable energy,” IEEE Access, vol. 12, June 2024, doi: 10.1109/ACCESS.2024.3413354.

[2]. A. Farakhor, M. Abapour, and M. Sabahi, “Design, analysis, and implementation of a multiport DC-DC converter for renewable energy applications,” IET Power Electron., vol. 12, pp. 465–475, Mar. 2019, doi: 10.1049/iet-pel.2018.5633.

[3]. S. Rostami, V. Abbasi, and N. Talebi, “Ultrahigh step-up multiport DC-DC converter with common grounded input ports and continuous input current,” IEEE Trans. Ind. Electron., vol. 69, no. 12, pp. 12859–12873, Dec. 2022, doi: 10.1109/TIE.2021.3131857.

[4]. K. Varesi et al., “Design and analysis of a developed multiport high step-up DC-DC converter with reduced device count and normalized peak inverse voltage on the switches/diodes,” IEEE Trans. Power Electron., vol. 34, no. 6, pp. 5464–5475, Jun. 2019, doi: 10.1109/TPEL.2018.2866492.

[5]. F. Nejabatkhah, S. Danyali, S. H. Hosseini, M. Sabahi, and S.M. Niapour, “Modeling and control of a new three-input DC–DC boost converter for hybrid PV/FC/battery power system,” IEEE Trans. Power Electron., vol. 27, no. 5, pp. 2309–2324, May 2012, doi:

10.1109/TPEL.2011.2172465.

[6]. L.-J. Chien et al., "Novel three-port converter with high-voltage gain," IEEE Trans. Power Electron., vol. 29, no. 9, pp. 4693–4703, Sep. 2014, doi: 10.1109/TPEL.2013.2297036.

[7]. H. Wu et al., "A family of multiport buck-boost converters based on DC-link-inductors (DLIs)," IEEE Trans. Power Electron., vol. 30, no. 2, pp. 735–746, Feb. 2015, doi: 10.1109/TPEL.2014.2329399.

[8]. L. Corradini et al., "Digital control of high-frequency DC-DC con-verters based on sliding mode current mode control," IEEE Trans. Power Electron., vol. 25, no. 1, pp. 105–117, Jan. 2010, doi: 10.1109/TPEL.2009.2039709.

[9]. M. Forouzesh, Y. P. Siwakoti, S. A. Gorji, F. Blaabjerg, and B. Lehman, "Step-up DC-DC converters: A comprehensive review of voltage-boosting techniques, topologies, and applications," IEEE Trans. Power Electron., vol. 32, no. 12, pp. 9143–9178, Dec. 2017, doi: 10.1109/TPEL.2017.2652318.

[10]. E. Amiri et al., "Multi-input high step-up DC-DC converter with independent control of voltage and power for hybrid renewable energy systems," IEEE Trans. Ind. Electron., vol. 68, no. 12, pp. 12467–12478, Dec. 2021, doi: 10.1109/TIE.2020.3044800.

[11]. Z. Li et al., "A single-stage three-port converter for PV-battery power systems," IEEE Trans. Power Electron., vol. 33, no. 6, pp. 5014–5027, Jun. 2018, doi: 10.1109/TPEL.2017.2740510.

[12]. M. D. Siddique et al., "A fault-tolerant multilevel inverter topology configured with three sources with improved performance in post-fault conditions," IEEE Trans. Power Electron., 2024.

[13]. M. Abbasi, "New nine-level common-ground multilevel inverter with switched-capacitor cell," IEEE Trans. Power Electron., 2025.

[14]. M. Jahnes and M. Preindl, "A novel three-phase partial power process-ing soft-switched inverter architecture," IEEE Trans. Power Electron., vol. 39, no. 12, pp. 16242–16255, Dec. 2024.

[15]. Z. Ye, E. Stolt, K. Surakitbovorn, and J. Rivas-Davila, "Broadband high-frequency power modulation with resistance regulation network," IEEE Trans. Power Electron., vol. 40, no. 11, pp. 16560–16571, Nov. 2025.

[16]. E. Stolt, M. Affolter, Z. Ye, and J. Rivas-Davila, "Current mode control for high frequency piezoelectric resonator-based DC–DC converters," IEEE Trans. Power Electron., vol. 40, no. 9, pp. 12730–12738, Sep. 2025.

[17]. Z. Ye, K. Surakitbovorn, C. H. Lin, and J. Rivas-Davila, "Design of a high-voltage low-ripple converter with high-frequency Dickson multipliers," IEEE Trans. Ind. Electron., vol. 72, no. 1, pp. 401–410, Jan. 2025.

[18]. R. Das and H.-P. Le, "Multi-inductor multi-output hybrid (MiMoH) converter for large conversion ratio and multiple outputs," in Proc. IEEE Appl. Power Electron. Conf. Expo. (APEC), Orlando, FL, USA, 2023, pp. 943–947.

[19]. Y. Li, F. Diao, and Y. Zhao, "A generic two-vector model predictive control for hybrid multilevel converters," IEEE J. Emerg. Sel. Topics Power Electron., doi: 10.1109/JESTPE.2021.3079927.